



# Combined multi-analytical approach for study of pore system in bricks: How much porosity is there?



Chiara Coletti <sup>a,b,\*</sup>, Giuseppe Cultrone <sup>b</sup>, Lara Maritan <sup>a</sup>, Claudio Mazzoli <sup>a</sup>

<sup>a</sup> Department of Geosciences, University of Padova, Via G. Gradenigo 6, 35131 Padova, Italy

<sup>b</sup> Department of Mineralogy and Petrology, Faculty of Science, University of Granada, Avda. Fuentenueva s/n, 18002 Granada, Spain

## ARTICLE INFO

### Article history:

Received 28 April 2016

Received in revised form 12 September 2016

Accepted 17 September 2016

Available online 24 September 2016

### Keywords:

Pore system

Pore morphology

Pore quantification

Combined techniques

2D and 3D digital image reconstruction

## ABSTRACT

During the firing of bricks, mineralogical and textural transformations produce an artificial aggregate characterised by significant porosity. Particularly as regards pore-size distribution and the interconnection model, porosity is an important parameter to evaluate and predict the durability of bricks. The pore system is in fact the main element, which correlates building materials and their environment (especially in cases of aggressive weathering, e.g., salt crystallisation and freeze-thaw cycles) and determines their durability. Four industrial bricks with differing compositions and firing temperatures were analysed with “direct” and “indirect” techniques, traditional methods (mercury intrusion porosimetry, hydric tests, nitrogen adsorption) and new analytical approaches based on digital image reconstruction of 2D and 3D models (back-scattered electrons and computerised X-ray micro-Tomography, respectively). The comparison of results from different analytical methods in the “overlapping ranges” of porosity and the careful reconstruction of a cumulative curve, allowed overcoming their specific limitations and achieving better knowledge on the pore system of bricks.

© 2016 Elsevier Inc. All rights reserved.

## 1. Introduction

Porosity and pore structure deeply affect the physical and mechanical properties and the durability of building materials. In bricks, the pore structure forms during production [1,2] and depends on the complex interaction of several factors, including mineralogical and chemical composition of the raw materials and the firing conditions (maximum firing temperature, soaking time, atmosphere), as widely demonstrated in the literature [3,4]. Pore shape, pore-size distribution and interconnections all affect the physical properties of bricks and are the most important parameters to be evaluated when predicting the durability of building materials [5]. Since open pores connect the interior parts of building materials with the external environment, determining fluid storage and circulation potential, the effectiveness of soluble salt crystallisation and freeze-thaw cycles all directly influence deterioration rates [6,7,8].

Proper characterisation of the pore structure of building materials, particularly that of bricks, is difficult because pores have very different shapes, sizes and connections, both among themselves and with the material surface [7]. By “pore connectivity”, we refer to total (or absolute) or effective porosity. Total porosity is the total volume of pores with respect to the bulk volume [9,10] and refers to closed and open pores, regardless of their degree of interconnection. Effective porosity

only refers to open and interconnected pores, accessible to the circulation of fluids or gases, and therefore constitutes the main pathway for damage [11]. Closed pores, although not affecting absorption and permeability, do influence the mechanical and physical properties of building materials, since they determine a decrease of density, strength, elastic modulus and hardness of a material [3,12,13,14].

A further criterion of pore classification is size. Although various categories of pore sizes are described in the literature [15], unanimous classification is difficult, mainly due to the differences in the ranges of macro-, meso- and micro-pores, still subject of animated discussion. Since porosity in bricks varies over a wide range, in this work pores will be classified according to the following categories [16]: micro-pores (with diameter smaller than 60  $\mu\text{m}$ ), meso-pores (with diameter between 60  $\mu\text{m}$  and 4 mm) and macro-pores (with diameter larger than 4 mm).

There are many methods for investigating and quantifying pore systems. However, the best description probably derives from comparisons among various techniques, each investigating only a restricted part of the whole system, due to specific limitations (e.g., in terms of pore-size interval, open or closed porosity) and instrumental setups [17,18,19,20,21,22,23,24,25].

A simple question such as “How porous is this sample?” really has a complex answer.

The multi-analytical approach adopted here combines “direct” and “indirect” techniques, traditional methods, and new analytical approaches based on digital image reconstruction of 2D and 3D models. “Indirect” techniques rely on the behaviour of the fluids used to evaluate

\* Corresponding author at: Department of Geosciences, University of Padova, Via G. Gradenigo 6, 35131 Padova, Italy.

E-mail address: [chiara.coletti@studenti.unipd.it](mailto:chiara.coletti@studenti.unipd.it) (C. Coletti).

the distribution, size and abundance of interconnected pores (effective or open porosity) inside the material. In this study, we used the following “indirect” methods: i) Mercury Intrusion Porosimetry (MIP), ii) Hydric Tests (HT) and iii) Nitrogen Adsorption (NA). “Direct” techniques allow good observation of the shape, distribution and abundance of open and closed pores. The direct methods used here were Scanning Electron Microscopy Back-Scattered Electrons (SEM-BSE) and Computerised X-ray micro-Tomography (micro-CT), coupled with Digital Image Analysis (DIA).

Each direct and indirect technique analyses a different range of pore size. To establish a connection among the various methods, “overlapping zones” were identified according to the image resolution established by SEM-BSE and micro-CT digital image analyses and a rather realistic representation of the pore system was achieved producing cumulative curves combining the contribute of each method.

In this study, we examined pore-size distribution and pore system structure in four commercial bricks, with various compositions of raw materials and firing temperatures. This information is essential in optimising new mix designs to produce bricks with suitable porosity, to be used both in restoration operations on ancient buildings and in modern ones, and in the definition of a protocol to quantify voids.

## 2. Sample Materials

Four types of bricks (R6, RSS, GP, N), produced by SanMarco-Terreal (Italy), were studied here. They were obtained from two types of clay, differing in the amount of carbonates: one was classified as carbonate-poor, as the amount of CaO + MgO was 8.84 wt%, and the other as carbonate-rich, with of CaO + MgO reaching 22.51 wt%. Both types were mixed with 10% of quartz sand (temper) and fired at different temperatures.

Two bricks were obtained from the carbonate-poor clay, according to firing temperature: sample R6 was fired at 600 °C and sample RSS at 950 °C. Two other bricks were produced from the carbonate-rich clay, samples GP and N, both fired at 1050 °C. About 15 wt% of hausmannite (Mn<sub>3</sub>O<sub>4</sub>) in fine powder was also added to sample N as grey dye, imparting a dark colour to the fired sample. The mineralogical composition of the bricks resulted to be related both to the firing temperature and to the initial composition of the greens [26]. The samples fired above 900 °C (RSS, GP and N) are characterised by quartz, wollastonite, gehlenite, plagioclase, K-feldspar, and diopside (Table 1). Brick

R6, fired at 600 °C, still contains phyllosilicates (chlorite and illite), and carbonates (calcite and dolomite). As for the feldspar, systematic differences were observed between bricks fired at 600 °C, where orthoclase from the raw material persists, and those produced at higher temperature (900–1050 °C), in which sanidine, the most stable high-temperature polymorph, formed.

Microstructurally, samples fired above 900 °C (RSS, GP and N) showed a partially melted groundmass and bridging, as well as reaction rims (corona-like structure) formed by new mineral phases, such as gehlenite and diopside, around carbonate inclusions in contact with quartz, feldspar, and the micromass (mainly amorphous phase derived from the phyllosilicates decomposition). In addition, physical-mechanical properties are closely dependent from the firing temperature, the nature of mineral phases, and the microstructure. The sample fired at 600 °C (R6) stands out for the highest structural anisotropy caused by the presence of phyllosilicates; by increasing firing temperature (bricks RSS, GP and N), samples became texturally more homogeneous and less anisotropic, as attested by the increasing ultrasonic wave velocities, and the formation of amorphous and new silicate phases, which both improved mechanical features. The evidence of a greater resistance and lower anisotropy for brick N compared to brick GP, produced with the same raw clay material and fired at the same temperature, suggests that the addition of hausmannite as dye, increased vitrification of the former fired brick [26]. The chemical-mineralogical characteristics and physical-mechanical features of these bricks are described in detail in Coletti et al. [26] and summarized in Table 1.

## 3. Analytical Techniques

### 3.1. Mercury Intrusion Porosimetry (MIP)

Mercury Intrusion Porosimetry (MIP) is a powerful technique used to evaluate open porosity (interconnected pores) and pore-size distribution in the range from 0.003 to 350 µm.

Since mercury is a non-wetting liquid, it does not spontaneously penetrate pores by capillary action, but must be forced by external pressure. The required pressure is inversely proportional to the size of the pores. Mercury fills larger pores first and, as pressure increases, smaller ones. Assuming a contact angle of 130° and a surface tension of 485 dyne cm<sup>-1</sup>, a pressure of 414 MPa is required for mercury to access pores as small as 0.003 µm.

**Table 1**

Summary of mineralogical and physical-mechanical characteristics of the bricks. Type of clay, use of additives, and firing temperatures are also reported.

	Additives (dye)	Firing T (°C)	Brick name	Mineral phases	Micro-structure	Mechanical features	Durability
Carbonate-rich clay	–	1050	GP	Newly formed silicates: diopside, wollastonite, gehlenite, sanidine Amorphous phase	Rather homogeneous structure Bridging Reaction rims	Improved mechanical features	Damage only along edges Good behaviour
	Mn <sub>3</sub> O <sub>4</sub>	1050	N	Newly formed silicates: diopside, bustamite (Mn-wollastonite), gehlenite, sanidine Amorphous phase	Rather homogeneous structure Bridging (Mn <sub>3</sub> O <sub>4</sub> increases the vitrification level) Reaction rims (widespread presence of bustamite crystals)	Highest load resistance	Damage only along edges Good behaviour Lowest weight loss
Carbonate-poor clay	–	600	R6	Persistence of phyllosilicates (illite and chlorite) and carbonates (calcite and dolomite) from the clay	Incipient melting  Absence of vitrification in the matrix High anisotropy	Low compactness	Loss of fragments and development of fissures and cracks
	–	950	RSS	Lack of reaction structures Newly formed silicates: diopside, wollastonite, gehlenite, sanidine	Rather homogeneous structure Partially melted groundmass and bridging Reaction rims	Intermediate mechanical features	Damage only along edges Good behaviour

Pressure intrusion data are provided by the porosimeter, which determines volume and size distributions according to the Washburn equation [27]:

$$PL + PG = 4\sigma \cos\theta/2D_p$$

where PL is the pressure of the liquid (in this case, mercury), PG the pressure of the gas in the pores (approximated to 0 atm in initial vacuum conditions),  $\sigma$  the surface tension of the liquid,  $\theta$  the contact angle of intrusion of the liquid (generally between 135° and 142° for mercury) and  $D_p$  is the pore diameter.

Although MIP is widely used, it does have two important limitations: the assumption that pores are perfectly cylindrical in shape, and that mercury moves from larger pores to smaller ones, discarding the opposite case, i.e., pores with the so-called “ink-bottle” morphology [28]. Therefore, mercury enters voids at a pressure determined only by the size of their entry points, and not the true size of the pore itself [29]. In addition, at high intrusion pressures (exceeding 414 MPa) pore structure may be damaged [22], distorting the pore range distribution [26] with an artificial increase in the small pore fraction [18].

The equipment used in this study was a Micromeritics Autopore III apparatus, model 9410, generating a maximum pressure of 414 MPa. Samples of approximately 2 cm<sup>3</sup> were freshly cut and oven-dried for 24 h at 110 °C before being analysed.

### 3.2. Hydric Tests (HT)

Hydric tests (HT) consisted of a series of measurements, such as water absorption and drying. Free and forced water absorption [31] and drying [32] were determined on three cube-shaped samples (with sides of 50 mm) for each brick type. The water absorption test consisted of determining the percentage of water absorbed by the mass of a sample over time. First, the samples were dried at 100 °C in an electric oven to determine their dry mass, and then completely immersed in water at controlled room temperature (20 °C) and relative humidity (30%). The samples were then periodically weighed (several times during the first hour and then once every 24 h) until they reached constant mass. The quantity of adsorbed water was the free water absorption ( $A_f$ ). Samples were then saturated with water under vacuum for 24 h, weighed and dried, to determine their capacity and velocity to lose water. Environmental conditions (temperature and relative humidity) were monitored and samples were weighed at the same frequency used to determine water absorption until constant mass was reached. For the purpose of this work, the following hydric parameters were calculated: open porosity (na); degree of pore interconnection ( $A_x$ ) [1,33].

Open porosity (na) was calculated as:

$$na = [(M_s - M_0)/(M_s - M_H)] \times 100$$

and the degree of pore interconnection ( $A_x$ ) was calculated as:

$$A_x = [(A_f - A_1)/A_f] \times 100$$

where  $M_0$  is the mass of the dried sample,  $M_s$  the mass of the sample saturated with water under vacuum,  $M_H$  the hydrostatic weight of the sample saturated with water under vacuum,  $A_1$  free water absorption and  $A_f$  forced water absorption.

Capillarity rise [33] was determined on three prism-shaped samples (25 × 25 × 120 mm) for each brick type, and weighed following the same timing used for water absorption and drying. Capillarity rise coefficient  $K_s$  was calculated as:

$$K_s = [(M_C - M_0)/A\sqrt{t}]$$

where  $M_0$  is the mass of the dried sample,  $M_C$  the amount of water absorbed at time  $t$ , and  $A$  the surface area of the sample (in cm<sup>2</sup>) in

contact with water. This method too, although widely adopted to measure the porosity of building materials, has some limitations. Unlike mercury, water is a wetting liquid which spontaneously penetrates open pores without requiring an external driving force. In the case of this study, brick is a material with a good aptitude for absorbing water and a high degree of wettability, but, although this method yields data on total effective porosity and the extent of pore interconnections, it does not describe pore-size distribution.

### 3.3. Nitrogen Adsorption (NA)

Nitrogen adsorption was used to determine brick porosity in the range (in diameter) between 0.0002 and 0.3 μm. Sorption isotherms were obtained at 77 K, on a Micromeritics Tristar 3000 in continuous adsorption conditions. Prior to measurement, samples were heated at 130 °C for 24 h and outgassed to 10<sup>-3</sup> Torr on a Micromeritics Flowprep. The total pore and micro-pore volumes of the samples were calculated by  $t$ -plot analysis. The Barret-Joyner-Halenda (BJH) method was used to obtain pore-size distribution curves.

Nitrogen adsorption (at 77 K) is the most widely used method to investigate the smallest pores in materials. The amount of adsorbed gas by the surface material is measured at discrete pressure ( $P$ ) steps over equilibrium pressure ( $P/P_0$ ), at constant temperature and at a value of  $P_0$  which corresponds to condensation pressure. Nitrogen fills the smallest micro-pores first, due to their larger adsorption potential at low relative pressure; as gas pressure increases, mono- and multi-layer adsorption occurs in the largest micro-pores. During the experiment, pressure was increased up to condensation (adsorption branch), followed by reduction of pressure ( $P_0$ ) (desorption branch); these data are reported as adsorption isotherms. The conventional technique makes discontinuous point-by-point measurements. The shape of the isotherms and their hysteresis patterns provided information on the types of pores present in the materials. Isotherms were classified according to the IUPAC nomenclature into six types (Types I–VI) [34]. There were four hysteresis patterns (H1–H4), characterising various meso-pore shapes [11].

Quantitative description of porosity was obtained by calculating total pore volume as follows [11]:

$$V_{liq} = (P_a V_{ads} V_m)/RT$$

where  $V_{liq}$  is the volume of adsorbed liquid N<sub>2</sub>,  $P_a$  the environmental pressure,  $V_{ads}$  the volume of adsorbed vapour,  $V_m$  the volume of N<sub>2</sub> adsorbed as a monolayer,  $R$  the gas constant, and  $T$  the temperature expressed in K.

Average pore radii ( $r_p$ ) were estimated from the pore volume, assuming cylindrical pore geometry, and expressed as:

$$r_p = (2 V_{liq})/S$$

where  $V_{liq}$  is N<sub>2</sub> liquid adsorbed and  $S$  the specific surface area.

Although nitrogen adsorption is widely used to determine the porosity of various materials, especially those characterised by micro-pores, this method necessarily assumes that: i) pores are rigid and cylindrical, and ii) the meniscus curvature of the fluid depends on pore dimensions (Washburn equation). Physical phenomena may significantly affect the adsorption isotherm and lead to incorrect pore-size estimation [35]. Hysteresis loops are also often observed, generally associated with the occurrence of meso-pores, since desorption paths may depend on percolation effects or channel variations in pore diameters. These assumptions prevent accurate description of both pore-size distribution and pore shapes. The method is fully reliable when pore structure is already known, but its results are questionable when applied to materials with complex and undetermined pore structure [36].

### 3.4. 2 Digital Image Analysis of SEM-BSE Images

New analytical approaches have greatly advanced our knowledge on pore structure and distribution through digital image analysis (DIA). High-resolution SEM-BSE study on thin section is a suitable alternative to traditional optical methods and is efficient in quantifying petrographic features and the porosity of geo-materials.

Porosity can be calculated from a binarised BSE image as the ratio of the number of pixels corresponding to the pores (pore-pixels) over the entire area of interest (AOI):

$$P_T = N_{pp}/(N_{pp} + N_{sp})$$

where  $N_{pp}$  is the number of pore-pixels (black) and  $N_{sp}$  that of solid-pixels (white). Pore-size distribution was calculated by dividing pores into the various classes of minimum Feret diameters (minFeret) calculated with ImageJ, the public domain Java image processing program [37].

The DIA of SEM-BSE images is a quite simple method for quantifying the total porosity, shape and size of pores, but the results may be influenced by instrumental conditions and settings are not always completely controllable. For instance, possible variations in grey-scale levels due to different contrast and brightness settings may affect the correct identification of pore/matrix and pore/temper interfaces. Although DIA is a direct technique, i.e., it can describe pore shape, some geometric information is lost, since the Feret diameter is a simplification which prevents complete description of empty spaces.

In this study, SEM-BSE images (1280 × 1024 pixel) were acquired with a CamScan MX 2500 microscope, equipped with a LaB<sub>6</sub> cathode, operating at 20 kV, working distance (WD) of 20 mm at a magnification of 50×, and 18 mm at a magnification of 500×. The two magnifications were adopted to study the pore system on differing scales in terms of the representativity of the investigated area with respect to a given interval of pore size. SEM-BSE grey-scale images were processed by ImageJ, reducing the noise and converting them into binary images (black and white) by thresholding. Information was grouped into two “classes” (black = pores; white = ground-matrix and grains of temper) [38,39,40]. For each class, training pixels were selected from specific regions of interest (ROI). Image segmentation (classification of each pixel) was performed on the basis of the ROI. In order to automate threshold selection and limit operator subjectivity, supervised classification was created with MultiSpec3.3© software. Total porosity was derived by counting the black pixels in the binary images. In order to increase representativity, digital imaging was performed on merged panoramic images obtained by stitching together 30 overlapping images at a magnification of 50× (resulting total area of the stitched image ~100 mm<sup>2</sup>) and 240 overlapping images at 500× (total area of the stitched image ~10 mm<sup>2</sup>).

### 3.5. 3D Digital Image Analysis by Computerised X-ray Micro-Tomography

Computerised X-ray micro-Tomography (micro-CT) 3D imaging, like SEM-BSE 2D digital imaging, is quite often used, since it allows examination of the internal structure of materials, including porosity.

Micro-CT analyses were performed on cores (diameter = 8 mm, length = 20 mm) on a bench-top Skyscan 1172 micro-CT scanner (Bruker®). The scanner is equipped with a Hamamatsu 100/250 microfocus X-ray source, operating at an acceleration voltage of 74 kV and a beam current of 133 μA, with a Hamamatsu C9300 10 megapixel camera (pixel size 8.5 μm) filtered by 0.5 mm Al foil. Projection images were acquired every 0.3° over 360° rotation with exposure time of 2500 ms and camera binning of 2 × 2, averaging 8 frames in vertical random movement mode to minimize noise, and connecting 3 scans to cover the entire vertical length of the cores. The run time for each scan was about 21 h. Cross-section slices were reconstructed from raw projection images with the NRecon software (Bruker®), with

application of thermal correction, misalignment compensation, ring artefact reduction and beam hardening correction, yielding voxel edges of 6 μm, corresponding to a minimum volume unit (voxel) of 216 μm<sup>3</sup>. Since in micro-CT images grey-scale values are proportional to the X-ray attenuation coefficients, which is a function of the mean atomic number of the specific voxel, porosity was segmented by thresholding tomographic images with the CT-Analyser software (Bruker®), which yielded binary image stacks.

After segmentation, porosity was calculated as the ratio of the number of voxels of the pores (pore-voxels) to the total volume of interest (VOI) [41] as follows:

$$P_T = N_{pv}/(N_{pv} + N_{sv})$$

where  $N_{pv}$  is the number of pore-voxels (white) and  $N_{sv}$  is the number of solid-voxels (black).

Pore structure can be analysed after idealised geometric discretisation of pore spaces in pore bodies and throats [41]. Here, pore-size distribution was described according to the structural thickness parameter obtained from 3D plug-in analysis of SkyScan CT-Analyser (CTAn) software package (Bruker®). The basic idea behind this approach is to skeletonise all pore bodies to identify their medial axes, and then calculate the chamfer distance from each voxel along them by sphere fitting [42,43]. Structural thickness distribution is therefore a measure of pore-size distribution.

CTAn also performs individual object analysis, thus allowing correlations between pore body volume and Sauter diameter ( $S_d$ ), defined as the diameter of the sphere with the same volume/area ratio of a given particle:

$$S_d = 6 \times (\text{Volume object}/\text{Area object})$$

The CTVox software (Bruker®) constructed realistic 3D visualizations of scanned objects.

The limitations of the DIA on micro-CT images are similar to those observed in DIA on SEM-BSE images. Although several filtering corrections were applied, the results may still be affected by limitations in instrumental settings. In addition, visual selection of proper thresholds during the binarisation process to separate pore bodies from solids inevitably introduces operator subjectivity bias. Although this technique can reconstruct the true 3D structure of pore bodies including closed pores, pore shape is affected by a certain degree of approximation, as it is generally unable to resolve porosity components smaller than about 6 μm [6].

## 4. Results and Discussion

### 4.1. MIP Measurements vs. Hydric Properties

MIP data, combined with information from hydric tests, allowed us to study water flux in bricks in relation to their pore-size distribution. The MIP curves show that all bricks have critical pore size between 1 and 2 μm (Fig. 1), but differ in pore-size distribution and threshold pore diameter (first inflection point in the cumulative mercury intrusion curve). Bricks fired at the highest temperature from a carbonate-rich clay (GP and N) have unimodal porometric curve distribution with both critical pore sizes and threshold pore radii (Fig. 1a, b) lower than the other bricks fired at lower temperature from a carbonate-poor clay (RSS and R6), which also shows a larger shoulder in the range 0.1–1 μm (Fig. 1c, d). In order to quantify these differences within the micro-porosity, the fraction below 0.1 μm was calculated and compared among samples. As expected, bricks fired above 950 °C (GP, N and RSS) are very similar, with lower percentages (0.45%, 0.99% and 0.83% respectively) than the brick fired at low temperature (R6), in which pores under 0.1 μm represent 5.72% of the total porosity (Table 2), and

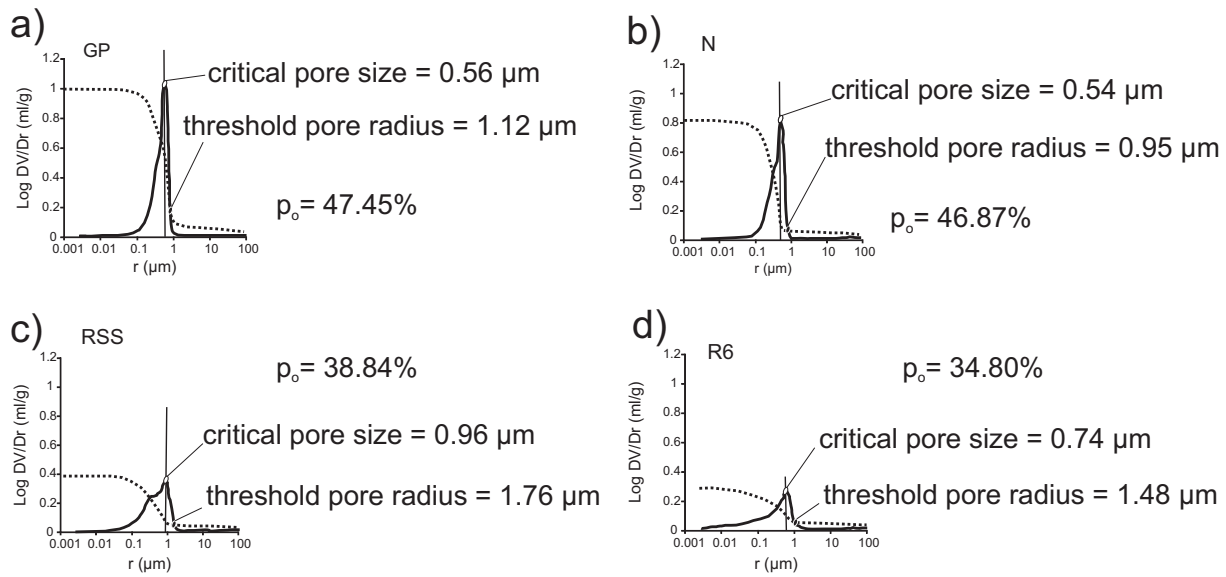


**Fig. 1.** Pore-size distribution curves of bricks in log differential intruded volume ( $\text{ml g}^{-1}$ ) vs. pore radius ( $\mu\text{m}$ ) diagram and relative cumulative curves (dotted lines) obtained by mercury intrusion porosimetry. a) GP (1050 °C); b) N (1050 °C); c) RSS (950 °C); d) R6 (600 °C).

the average pore radius ( $0.06 \mu\text{m}$ ) is smaller than the other ones (GP:  $0.33 \mu\text{m}$ ; N:  $0.24 \mu\text{m}$ ; RSS:  $0.29 \mu\text{m}$ ) (Table 2).

The percentage of open porosity ( $p_o$ ) determined by MIP was influenced by the quantities of carbonates in the clay materials [7]. Bricks GP and N, produced with a carbonate-rich clay, have the highest values of open porosity (47.45% and 46.87%, respectively); the slight difference

observed among them may be related to the addition of  $\text{Mn}_2\text{O}_4$ . As for the bricks produced from carbonate-poor clay, the lowest open porosity was observed in that fired at the lowest temperature (R6: 34.80%) (Table 2). All samples display similar patterns of the absorption curves (Fig. 2a). The sample with the highest free and forced water absorption values ( $A_f = 27.63\%$ ,  $A_f = 28.71\%$ ) is GP, followed by N. RSS showed

**Table 2**  
Main parameters related to porosity measured on bricks GP, N, RSS and R6 as obtained from Mercury Intrusion Porosimetry (MIP), Hydric Test (HT),  $\text{N}_2$  Adsorption (NA),  $50\times$  SEM-BSE images,  $500\times$  SEM-BSE images, and micro-CT.

		Bricks			
		Carbonate-rich clay		Carbonate-poor clay	
		GP (1050 °C)	N (1050 °C)	RSS (950 °C)	R6 (600 °C)
MIP	Total open porosity (%)	47.45	46.87	38.84	34.80
	Critical pore size ( $\mu\text{m}$ )	0.56	0.54	0.96	0.74
	Threshold pore radius ( $\mu\text{m}$ )	1.12	0.95	1.76	1.48
	Porosity below $0.1 \mu\text{m}$ (%)	0.45	0.99	0.83	5.72
	Porosity below $1 \mu\text{m}$ (%)	27.94	33.01	20.11	22.95
	Porosity below $6 \mu\text{m}$ (%)	46.03	45.27	37.11	32.58
	Porosity between 1 and $6 \mu\text{m}$ (%)	18.09	12.26	17.00	9.63
HT	Average pore radius ( $\mu\text{m}$ )	0.33	0.24	0.29	0.06
	Total open porosity (%)	41.36	40.56	37.52	31.14
	Free absorption $A_f$ (%)	27.63	25.08	21.57	17.36
	Forced absorption $A_f$ (%)	28.71	25.85	23.28	17.88
	Pore interconnection degree ( $A_x$ )	3.76	2.98	7.35	2.91
NA	Capillarity rise ( $K_c$ )	0.43	0.33	0.30	0.16
	$t$ -Plot micro-pore volume ( $\text{cm}^3/\text{g}$ )	−0.00014	0.000035	0.000129	0.001006
SEM $50\times$	BJH desorption volume ( $\text{cm}^3/\text{g}$ )	0.00445	0.009709	0.002686	0.244700
	Total porosity (%)	10.96	11.77	13.09	5.68
	minFerret (max value; $\mu\text{m}$ )	800	378	1450	428
SEM $500\times$	Anisotropy (max value)	13.64	10.98	16.03	16.02
	Total porosity (%)	25.59	24.99	24.43	15.68
	minFerret (max value; $\mu\text{m}$ )	205	300	225	159
	Porosity between 1 and $6 \mu\text{m}$ (%)	7.67	7.51	7.24	5.59
	Porosity above $6 \mu\text{m}$ (%)	17.28	16.74	16.51	9.50
Micro-CT	Average mean value (minFerret)	0.90	0.85	1.00	0.70
	Pore anisotropy (max value)	33.36	33.36	38.29	91.39
	Total porosity (%)	15.64	9.89	26.85	9.08
	Porosity between 6 and $20 \mu\text{m}$ (%)	7.85	3.75	14.72	3.67
	Mean structural thickness ( $\mu\text{m}$ )	46.92	32.68	24.96	43.23
	Max structural thickness ( $\mu\text{m}$ )	534	330	258	330
	Sauter diameter (max value; $\mu\text{m}$ )	231	149	40	231
	Structure model index (0 = plate/3 = rod)	2.67	2.67	2.63	2.67
	Sphericity (0–1)	0.79	0.79	0.81	0.79
	Fractal dimension	2.32	2.89	2.99	2.88

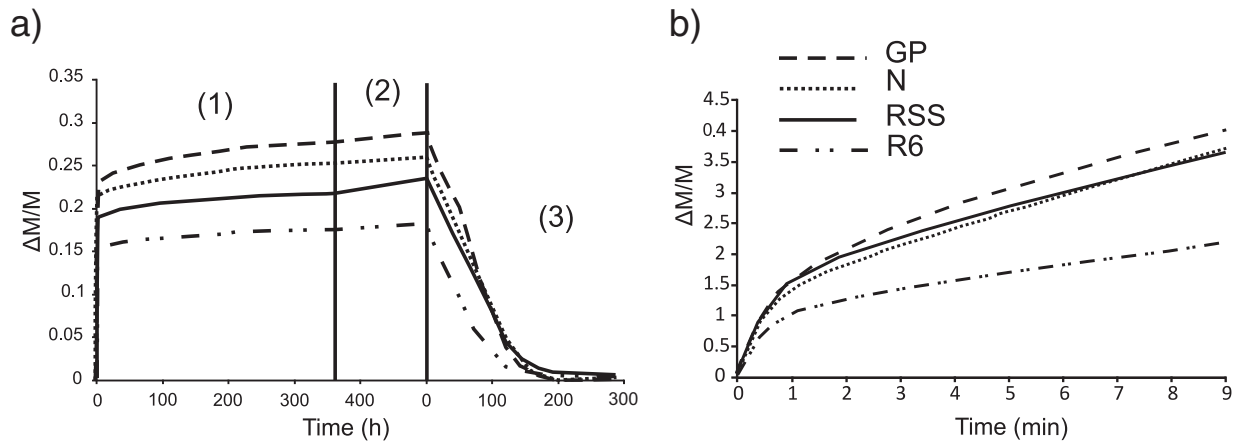


**Fig. 2.** a) Results from hydric tests: free water absorption (1), forced water absorption (2), drying (3) of bricks. Weight variation ( $\Delta M/M$ ) vs. time (h); b) results from capillarity test (until 9th minute of test). Weight variation ( $\Delta M/M$ ) vs. time (min).

lower water absorption compared to N ( $A_i = 21.57\%$ ,  $A_f = 23.28\%$ ), but is the sample with the worst pore connection system ( $A_x = 7.35$ ) (Table 2). This indicates the existence in RSS of pores with small access, which hinders water movement inside the brick. R6 is very different from the others, with a low attitude towards absorbing water ( $A_i = 17.36\%$ ,  $A_f = 17.88\%$ ) and is characterised by the best pore interconnections ( $A_x = 2.91$ ) (Table 2).

The results of the capillarity test emphasised the trend followed by samples submitted to free water absorption (Fig. 2b). GP is the most susceptible to capillarity rise ( $K_s = 0.43$ ), whereas R6 has the lowest  $K_s$  value ( $K_s = 0.16$ ) (Table 2). There is a close relationship between capillarity rise and pore-size distribution determined by MIP. GP, fired at 1050 °C, displayed the highest capillarity, determined by the highest number of pores, corresponding to the critical size for capillarity rise (0.1–10  $\mu\text{m}$ ). Instead, R6, fired at 600 °C, has a large number of pores smaller than 0.1  $\mu\text{m}$  and is the least affected by capillary action (Table 2).

#### 4.2. Nitrogen Adsorption Behaviour

The NA isotherms of the samples belong to type IV, with H3 hysteresis loops according to the IUPAC classification [34,44], reflecting the meso-porous nature of the materials [45]. Although the hysteresis loop is usually associated with capillary condensation in meso-pore structures and involves complications in correct characterisation of porosity, it can provide important information on pore structure and morphology [46]. In particular, hysteresis type H3 can be determined by the presence of pores between aggregates of plate-like particles or assemblages of slit-shaped pores and usually provides a reliable assessment

of pore-size distribution. The different behaviour in adsorption and desorption is evident in the relative pressure interval ( $P/P_0$ ) between 0.4 and 0.5, where the desorption branch drops [36]. This phenomenon was particularly evident in bricks R6 and N, which were also the samples with the highest gas volumes intruded (Table 2). R6 provided the isotherm with the highest plateau at lower relative pressures, whereas N displayed intermediate values, and RSS and GP the lowest almost overlapping adsorption isotherms (Fig. 3a). In general, the  $t$ -plot micro-pore volume (for pores smaller than 0.001  $\mu\text{m}$ ) in all the bricks is relatively low, as also confirmed by the pore-size distribution calculated according to the BJH method (range 0.001–0.15  $\mu\text{m}$ ), indicating that sample porosity is mainly concentrated in the meso- and macro-pore ranges. R6, fired at the lowest temperature, provided the highest micro-porosity (BJH desorption volume: 0.24470  $\text{cm}^3/\text{g}$ ), followed by N (0.009709  $\text{cm}^3/\text{g}$ ), GP and RSS (0.004450 and 0.002686  $\text{cm}^3/\text{g}$ , respectively) (Table 2). Plots of BJH pore-size distribution of the NA desorption curves (Fig. 3b) showed that most of the porosity ranges between 0.003 and 0.005  $\mu\text{m}$ , with brick R6 having the highest peak in this range, followed by N, GP and RSS (Fig. 3b), and the occurrence of an evident shoulder between 0.010 and 0.015  $\mu\text{m}$  (Fig. 3b). These data confirmed previous MIP observations; in particular: i) porosity is characterised by smaller pores in R6 (fired at 600 °C) than in the other bricks; ii) the two samples fired at 1050 °C (N and GP) differ, smaller pores being more abundant in that produced with the addition of  $\text{Mn}_3\text{O}_4$ . In this latter, the higher amount of smaller pores, can derive from different grain packing due to the addition of hausmannite in a very fine powder and/or to the internal micro-structure of the Mn-oxides formed during firing and showing a porous micro-dendrite-like structure [26] (Fig. S1).

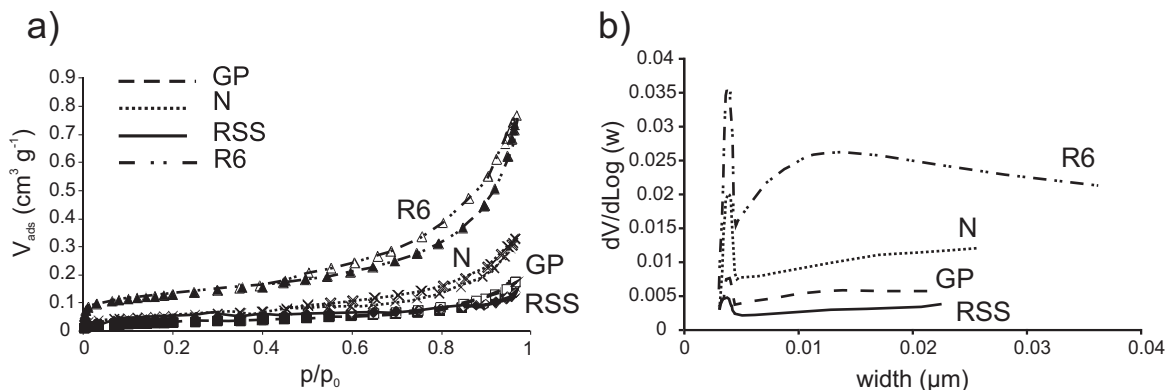


**Fig. 3.** a)  $\text{N}_2$  isotherms of bricks: volume adsorbed  $V_{\text{ads}}$  ( $\text{cm}^3/\text{g}$ ) vs. relative pressure ( $p/p_0$ ); b) pore-size distribution curves: log differential intruded volume ( $\text{cm}^3/\text{g}$ ) vs. pore width ( $\mu\text{m}$ ).

#### 4.3. 2D Image Processing

A series of SEM back-scattered images at magnifications of  $50\times$  and  $500\times$  were acquired for all bricks. In both series of images, it was decided to identify pores with a minimum of 2 pixels (threshold limit) in order to solve problems due to variations in grey-scale and to pore-matrix/temper interfaces. These limits constrain the threshold resolution to  $5\ \mu\text{m}$  for images obtained at  $50\times$  and to  $0.5\ \mu\text{m}$  for those at  $500\times$ .

The need to work with merged panoramic images is due to the high complexity and heterogeneity of the pores, in terms of both sample size and distribution, and thus overcoming the poor representativity of single images. Before analysing panoramic images, therefore, comparisons of the porosity values determined from single images were carried out on brick R6. Fig. 4a shows the high variability of the total porosity of

30 single images; the dotted red line shows the value of total porosity calculated over the panoramic image. For example, image C (Fig. 4b) has the highest porosity (8.29%), image A the lowest (1.51%) and image B is intermediate (6.13%). These significant discrepancies can also be seen in the pore-size distribution (Fig. 4c): image A has a high number of small pores and C the opposite, with many large pores; B contains both small and large pores. This confirms the inhomogeneous distribution of porosity and its complexity, but it also indicates that the presence of larger pores determines higher porosity values.

This can be also observed when the percentage of the largest pore (Largest Pore Area/Total Image Area, expressed in %) in each image is compared with the total porosity of that image ( $P_s$ ), normalised to the total porosity of the panoramic image ( $P_p$ ) according to the following equation:  $(P_s - P_p) / P_p$  (Fig. 4d).

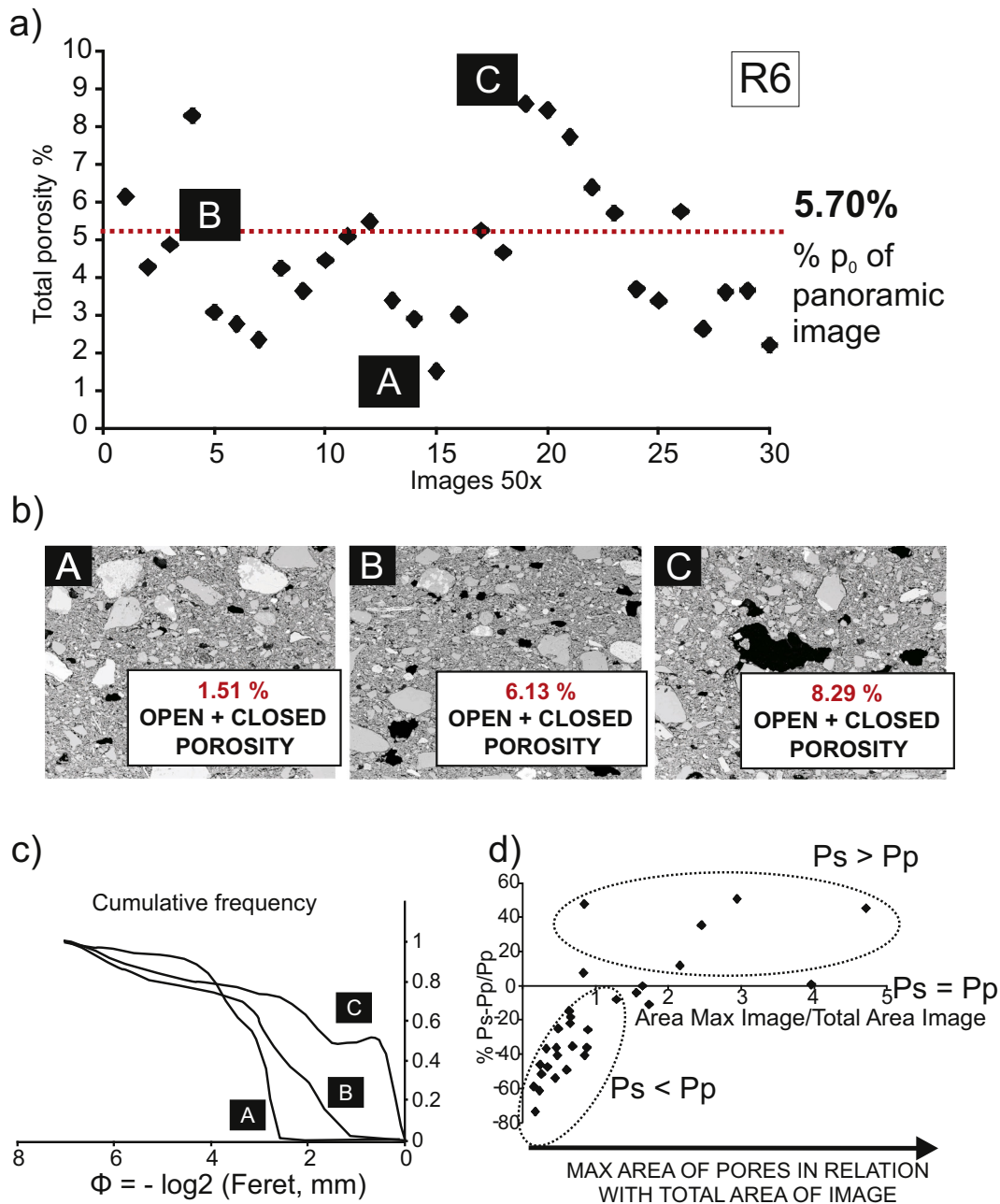


**Fig. 4.** 2D DIA of sample R6 (as example): a) Comparison between total porosity calculated for single SEM-BSE  $50\times$  images (filled diamonds) and total porosity obtained from merged panoramic image (red dotted line); b) three single images of sample R6, showing high variability of porosity; c) cumulative frequency plots of same three single images; d) distribution of single images (filled diamonds) considering maximum pore area in image with respect to total area of image (For interpretation of the references to colour in this figure legend, the reader is referred to the web version of this article).

Table 2 lists the values of total porosity for all bricks, calculated on the panoramic images taken at 50×. The sample with the highest value of total porosity is RSS (13.09%), followed by N (11.77%) and GP (10.96%), whereas R6 has the lowest value (5.68%) (Table 2). Images at 50× displayed larger variability among bricks in terms of largest pore size (max value) than those at 500× (Table 2). RSS had the largest isolated pores in the matrix, up to a minFerret diameter of 1450 μm.

When compared to other techniques, 500× SEM-BSE image analysis turned out to be particularly useful, since these images covered a similar range of pore-size distribution with respect to MIP. Total porosity from 500× images was always higher than that from 50×, although showing a similar trend among the samples, with bricks fired above 950 °C (GP, N and RSS) displaying higher porosity than that fired at low temperature (R6) (Table 2). Samples fired at higher temperatures (GP, N and RSS) had larger pores (up to 205, 300 and 225 μm, respectively), while R6, fired at a lower temperature, had smaller pores (up to 159 μm) (Table 2), confirming the influence of firing on pore size, since pores tend to increase in size when vitrification occurs [2]. The cumulative frequency distribution of pores was concentrated under minFerret diameters of 10 μm; in particular, in GP, N and RSS, about 47% of the pores fell in this range, although in sample R6 it was as high as 55.65% (Table 2), confirming MIP and NA values. The average value of pore diameters (minFerret) in R6 was lower (0.70 μm) than that of N (0.85 μm), GP (0.90 μm) and RSS (1 μm).

As pore shape can influence water storage, the effect of firing temperature on this parameter was substantial. An important shape factor is circularity, which can be used to describe the degree of asymmetry of a pore shape, calculated in 2D according to the following equation:

$$c = 4\pi (A / P^2)$$

where A and P are the area and perimeter of each pore, respectively. Circularity factor c fell between 0 (perfectly elongated shape) and 1 (perfectly circular shape). Circularity factors obtained from the segmented panoramic 50× images were also plotted against the corresponding minFerret values (Fig. S2). Pores with approximately circular shape (c approaching 1) were more abundant in samples fired at higher temperatures (GP and N). In particular, N had the greatest fraction of rounded pores. This observation was also confirmed in 500× images (Fig. S2).

The pore anisotropy was also evaluated by examining the ratio of maximum Feret diameter (maxFerret) with respect to minFerret. When

these parameters are very similar, particles are almost isotropic; when the ratio is higher than 1, particles are anisotropic (elongated). The pores of samples N and GP in both 50× and 500× images had the lowest ratios (Table 2), confirming that bricks fired at higher temperatures are characterised by more circular pores, matching circularity distribution.

#### 4.4. 3D Image Processing

After reconstruction, sufficient filtering and 3D thresholding, the stack of binarised images (Fig. 5) for each sample core underwent 3D analysis by CTAn. A 3D video reconstruction and a slideshow video are provided in Figs. S3 and S4. RSS displayed higher porosity (26.85%) than GP (15.64%), N (9.89%) or R6 (9.08%) (Table 2). As the voxel edge was 6 μm, the cumulative frequency curves of the structural thickness showed different pore-size distributions among the samples. Most of the pores fell in the range 6–20 μm (Table 2). When the largest measured pores (max structural thickness in Table 2) and the Sauter diameter are considered, a high variability is observed with respect to the maximum values obtained by 2D DIA on both 50× and 500× SEM-BSE images (Table 2). This indicates that large pores are highly anisotropic and randomly distributed in the samples.

In order to study the 3D morphology of pores, the Structure Model Index (SMI) was calculated, according to differential analysis of triangulated pore surfaces to quantify the structure model type, such as plate (SMI = 0) or rod (SMI = 3), or a mixture of the two (SMI between 0 and 3). Results showed very similar average values (Table 2), indicating that pores are approximately rod-shaped.

The sphericity (Sph) of a pore is defined as the ratio of the surface area of a sphere to the same volume as the given pore to the surface area of the pore:

$$\text{Sph} = \left( \sqrt[3]{\pi(6V)^{\frac{2}{3}}} \right) / S$$

where V and S are object volume and surface area, respectively. The maximum possible value for sphericity is 1, which corresponds to a perfectly spherical object. All samples have sphericity values close to 1 (Table 2).

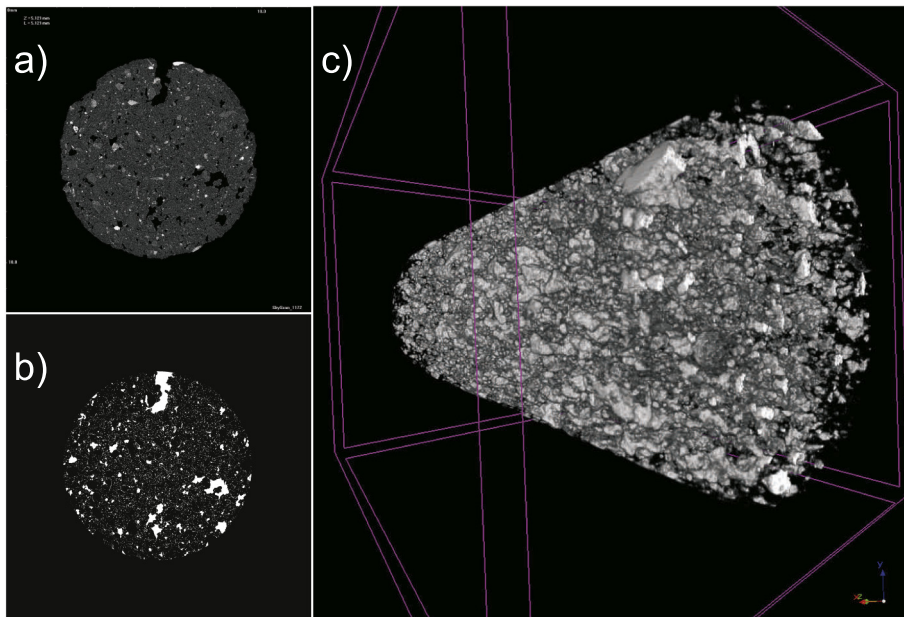


Fig. 5. One of the reconstructed m-CT images belonging to the stack of images used to produce the 3D model of the pore system (sample R6): a) grey tone reconstructed tomographic image; b) the same image binarised after segmentation (white areas correspond to pores); c) 3D model built from the stack of binarised images using the CTvox software (white volumes correspond to pores).

The Fractal Dimension (FD) is an indicator of the surface complexity of an object and has a dimension between 2 and 3. Our samples have FD between 2.32 (GP) and 2.99 (RSS), confirming the true fractal behaviour of the pore system (Table 2).

#### 4.5. Comparing Techniques: “Overlap” Method and Cumulative Curve Reconstruction

In order to compare the results from the various techniques, the porosity fraction pertaining to a specific “overlapping range” (OR) was extracted from the pore-size distribution curves of the various techniques used here (Fig. 6). Three overlapping pore ranges were examined: i) pores between 0.003 and 0.02  $\mu\text{m}$ , giving partial results extrapolated by MIP and NA; 2) pores between 0.5 and 6  $\mu\text{m}$ , giving partial results obtained from MIP and 2D DIA of 500 $\times$  SEM-BSE images; 3) pores between 6 and 100  $\mu\text{m}$ , giving partial results extrapolated by MIP, 2D DIA of 500 $\times$  and 50 $\times$  SEM-BSE images and micro-CT. Although these results indicate that all these techniques provide different porosity values within the same pore-size range (Table 3), similar patterns of pore-size distribution can be observed. In the smallest overlapping range (OR 1 in Fig. 6; 0.003–0.02  $\mu\text{m}$ ), pore quantification is quite similar when the results of the two techniques are compared, although the porosity values measured by NA are generally slightly higher (Table 3). This may be explained by recalling that this pore range is within the ideal investigation range of the NA technique rather than that of MIP.

Within the 0.5–6  $\mu\text{m}$  range (OR 2 in Fig. 6), there is a perfect match in the pattern of pore-size distribution obtained from MIP and 2D DIA of 500 $\times$  SEM-BSE images, although MIP always provided higher porosity values (Table 3). This difference may be explained considering the limitations of both these techniques. MIP tends to overestimate porosity in this range, because of the ink-bottle effect, which tends to underestimate real pore size. Instead, SEM-BSE images are a 2D representation of the pore system, so that DIA generally tends to underestimate total porosity. Nevertheless, samples show analogous trends from both the techniques, with the highest porosity in GP and the lowest in R6 (Table 3).

When we examined the range between 6 and 100  $\mu\text{m}$  (OR 3 in Fig. 6) the mismatch among results obtained with the different techniques (MIP, 2D DIA of SEM-BSE images, and micro-CT) was even more noticeable. MIP gave the lowest porosity, clearly affected by a strong ink-bottle effect in this dimension range, and the lack of accuracy approaching its upper limit of applicability. SEM-BSE images and micro-CT gave higher porosity estimates and did not follow the same pattern as MIP (Table 3). Porosity obtained by 2D DIA of 500 $\times$  SEM-BSE images and micro-CT is very similar in all the bricks, with the exception of brick RSS, for which micro-CT provided sensibly higher porosity values (Table 3). This discrepancy is probably due to the complexity of the pore system of this brick, characterised by very large but widely spaced pores, as

**Table 3**  
Porosity referred to specific “overlapping ranges” (OR) obtained with various analytical techniques. Abbreviations as in Table 2.

	Pore range (diameter, $\mu\text{m}$ )	Techniques	Bricks			
			Carbonate-rich clay		Carbonate-poor clay	
			GP (1050 °C)	N (1050 °C)	RSS (950 °C)	R6 (600 °C)
OR 1	0.003–0.02	MIP	0.04	0.15	0.00	1.91
		NA	0.44	0.87	0.26	2.26
OR 2	0.5–6	MIP	38.19	34.28	27.65	17.44
		SEM 500 $\times$	8.33	8.25	7.92	6.11
OR 3	6–100	MIP	0.88	1.01	1.17	1.28
		SEM 50 $\times$	7.87	9.64	4.24	3.44
		SEM 500 $\times$	14.10	13.67	13.61	7.74
		Micro-CT	13.26	9.38	26.64	8.32

also shown in the 50 $\times$  SEM-BSE images (Fig. S5). Interestingly, also the total porosity measured on 50 $\times$  SEM-BSE images, which has a threshold of about 5  $\mu\text{m}$ , is very similar to porosity above 6  $\mu\text{m}$  measured on 500 $\times$  SEM-BSE images and micro-CT (Table 2), giving confidence on 2D DIA, and suggesting that the latter magnification is sufficiently representative of the pore system, although obtained over a considerably smaller area. This also suggests that 2D DIA of 500 $\times$  SEM-BSE images is sufficiently reliable in describing both pore-size distribution and total porosity above 6  $\mu\text{m}$ , and most likely also down to about 1  $\mu\text{m}$ , a value which is sufficiently far from the 0.5  $\mu\text{m}$  lower limit imposed by the threshold on the minimum meaningful number of pixels on BSE images. This is particularly relevant because it allows accounting for the ink-bottle effect on MIP also below 6  $\mu\text{m}$ , possibly down to 1  $\mu\text{m}$ .

The values determined by MIP of the total open porosity ( $p_o$ ) are very similar, although always slightly higher, than those determined by HT (Table 2), suggesting that both these techniques are rather reliable in determining the total open porosity of the samples, which is mostly within their investigation range. The considerable difference between these values and those determined by micro-CT may be related to the lower limit of the pore size that can be investigated with the latter method, corresponding to a pore diameter of 6  $\mu\text{m}$ . Provided that micro-CT performs an accurate 3D reconstruction of the pore system above this threshold, in general with values of the total porosity reasonably similar to the pore fraction above 6  $\mu\text{m}$  obtained by 500 $\times$  SEM-BSE images and by 50 $\times$  SEM-BSE images, the observation that MIP assigns >95% of the total open porosity to pores with diameter below 6  $\mu\text{m}$  (Table 2), provides an evidence of the strong ink-bottle effect on the MIP description of the pore-size distribution. This is also confirmed by the values of the pore fraction in the interval 1–6  $\mu\text{m}$ , which are systematically higher for the MIP than for the 2D DIA of 500 $\times$  BSE-SEM images.

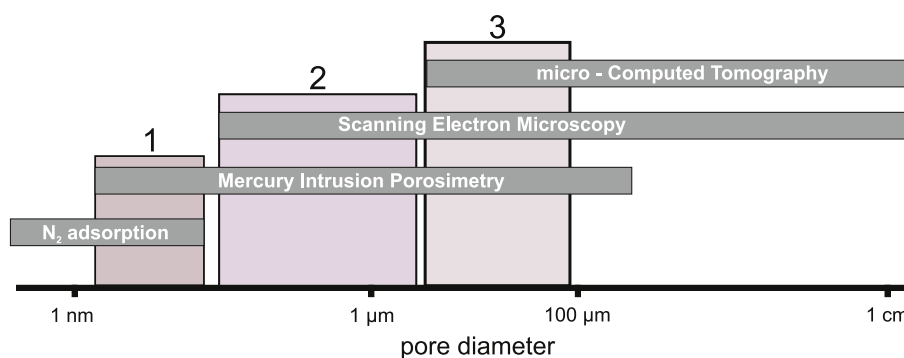


**Fig. 6.** Sketch of the three “overlapping ranges” (OR) identified for various analytical techniques. OR 1: 0.003–0.02  $\mu\text{m}$  (MIP and  $\text{N}_2$  adsorption); OR 2: 0.5–6  $\mu\text{m}$  (MIP and 500 $\times$  SEM-BSE images); OR 3: 6–100  $\mu\text{m}$  (MIP, 500 $\times$  SEM-BSE images and micro-CT).

Indeed, a considerable fraction of the pores assigned by MIP to the interval below 6 μm, at least corresponding to the total porosity determined by micro-CT or SEM-BSE images, should be referred to the interval

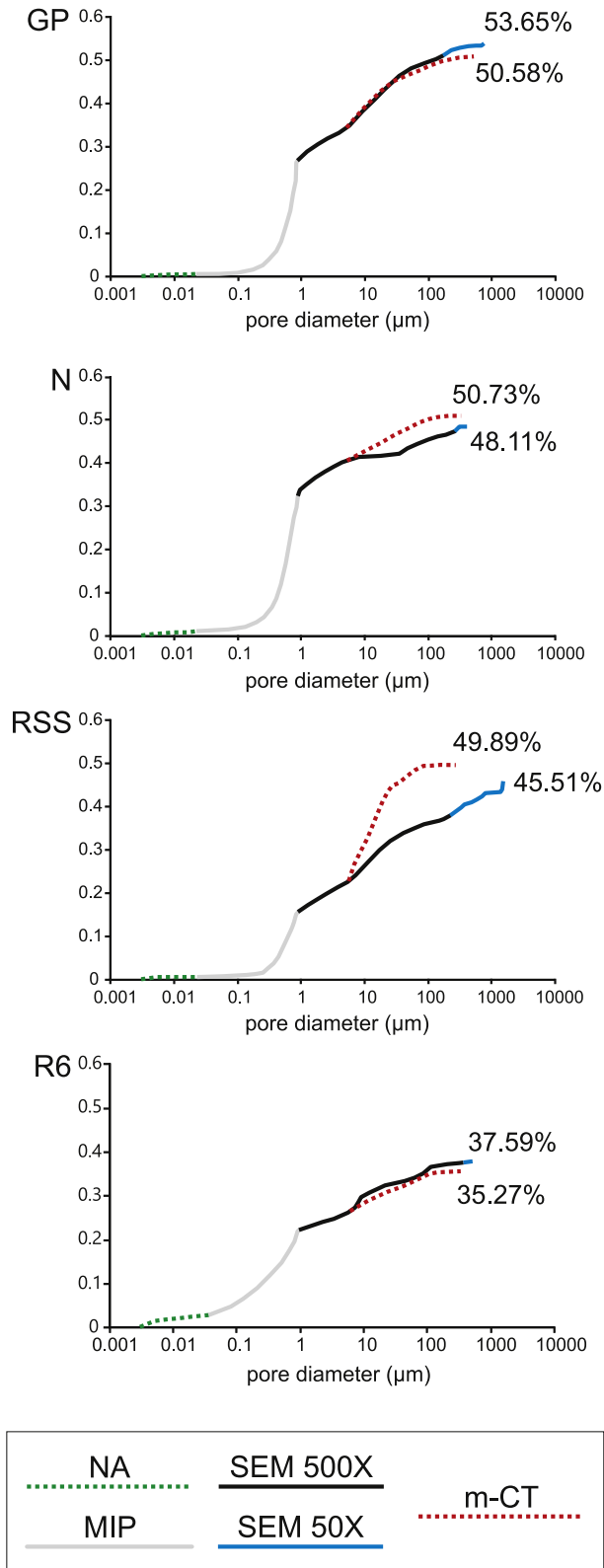


**Fig. 7.** Cumulative curves of the pore-size distribution based on nitrogen desorption (BHJ; 0.003 μm < Ø < 0.02 μm), mercury intrusion porosimetry (MIP; 0.02 μm < Ø < 10 μm), and image analyses (500×, 50× SEM-BSE images and micro-CT; Ø > 6 μm) (For interpretation of the references to colour in this figure legend, the reader is referred to the web version of this article).

**Table 4**

Total porosity obtained by adding the contribution from the various methods within specific pore-size intervals defined by the cut-off values described in the text. Abbreviations as in Table 2.

	Total porosity				
	NA + MIP + SEM 500×	NA + MIP + SEM 500× + 50×	NA + MIP + SEM 500× + micro-CT	MIP	HT
GP	51.84	53.65	50.58	46.83	41.36
N	47.95	48.11	50.73	43.23	40.56
RSS	38.86	45.51	49.89	40.23	37.52
R6	36.74	37.59	35.27	33.70	31.14

above 6 μm. Therefore, the fraction of pores below 6 μm should correspond to the difference between the total open porosity obtained by MIP and that provided by micro-CT or SEM-BSE images.

All this considered, a cumulative curve of the pore-size distribution was obtained for each sample by merging the results of the different techniques (Fig. 7), the single cumulative curves of which are reported in Fig. S6. Due to the overlapping pore-size ranges between couples of methods, the cumulative curves were calculated by *a priori* defining a pore-size cut off as a threshold limit between “adjacent” techniques. Each curve starts with the pattern determined by NA up to 0.02 μm, since for the studied sample NA provided adsorption volume up to this pore width (Fig. 3b). Pore size distribution pattern obtained by MIP follows. In order to minimize the distortion caused by the ink-bottle effect on the pore-size pattern, the limit between MIP and 2D DIA of 500× SEM-BSE images was set to 1 μm (Fig. 7). Above 6 μm, pore-size pattern may either consider the contribution of 500× SEM-BSE images and, when providing information on larger pores, also 50× SEM-BSE images, or that of micro-CT, obtaining two curves for each sample (Fig. 7). Total porosity obtained with these threshold values are similar to those measured with MIP and HT (Table 4), and follow the same trend: carbonate-rich bricks are the ones with the highest total porosity (Table 4) and samples fired at lower temperature (in particular R6) display a higher amount of small pores (Fig. 7).

**5. Conclusions**

The combination of various methods successfully provided reliable characterisation of the pore system in bricks, together with better understanding of the specific limitations of the different techniques.

The results obtained from various techniques, and the critical analysis of “overlapping ranges” allowed more realistically describing the characteristics of the whole pore system and its complexity, and highlighting the specific limitations of the different analytical methods. The multi-analytical approach used here allowed us to describe in detail the relations among raw materials, firing temperatures and porosity. Bricks made with carbonate-rich clay and fired at high temperature (1050 °C), such as GP and N, display the largest volume of open pores, most likely produced by the decomposition of carbonate during firing. High firing temperature also favoured the development of large, rounded pores. Instead, porosity in R6, prepared with a carbonate-poor clay and fired at 600 °C, showed rather different features: pore shapes are more inhomogeneous and the volume of small pores is definitely higher. RSS, prepared with the same starting raw material as R6 and fired at 950 °C, showed intermediate features and the highest complexity of the pore system.

Moreover, the study clearly indicates that none of the analytical methods here adopted is able to describe the whole pore system adequately and completely. MIP permits a reliable quantitative estimate of the total open porosity, and provides values that are comparable with those obtained by HT, but returns unrealistic description of the pore-size distribution because of a strong influence of “ink-bottle” pores, the effect of which have been proven to be dramatic down to 1 μm, but certainly still affects pore-size distribution below 1 μm. Indeed, the excess of the total porosity derived from the cumulative

curves of Fig. 7 with respect to the total open porosity obtained by MIP (Table 4) is basically determined by the MIP overestimation of the volume of pores below 1  $\mu\text{m}$ . This is consistent with observations on different products such as cement-based materials [20,30]. NA obviously provides a small contribution to the determination of the total porosity in bricks, but describes a range of pores below the detection limit of other techniques. DIA on both SEM-BSE and micro-CT images provides good quantitative and morphological (pore size and shape) information to investigate the meso- and macro-pore system of ceramic materials, although cannot access an important fraction of the total porosity in the small meso-pore to micro-pore range.

Therefore, congruently to what observed by De Boever et al. [47] on natural stones (sandstones), the results we achieved show that only the combination of the various analytical methods can provide a realistic reconstruction of the pore system in materials such as bricks, characterised by complex pore structure over a wide range of pore size.

Supplementary data to this article can be found online at <http://dx.doi.org/10.1016/j.matchar.2016.09.024>.

## Acknowledgments

This study was funded by the Research Group RNM of the Junta de Andalucía and by the Research Project MAT2012-34473. The research benefited by funding from INPS - Gestione Ex Inpdap (Direzione Regionale Veneto), which provided the PhD "Doctor J" Grant over the period 2013–2015. The authors are grateful to SanMarco-Terreal Company, in particular to Franco Favaro and Francesco Stangherlin. We are also grateful to Gabriel Walton who revised the English text, and to two anonymous reviewers, whose comments substantially improved the manuscript.

## References

- [1] G. Cultrone, F. Madkourb, Evaluation of the effectiveness of treatment products in improving the quality of ceramics used in new and historical buildings, *J. Cult. Herit.* 14 (2013) 304–310.
- [2] D. Benavente, L. Linares-Fernández, G. Cultrone, E. Sebastián, Influence of microstructure on the resistance to salt crystallisation damage in brick, *Mater. Struct.* 39 (2006) 105–113.
- [3] G. Cultrone, E. Sebastián, K. Elerta, M.J. de la Torre, O. Cazalla, C. Rodríguez-Navarro, Influence of mineralogy and firing temperature on the porosity of bricks, *J. Eur. Ceram. Soc.* 24 (2004) 547–564.
- [4] R. Sobott, K. Bente, M. Kittel, Comparative porosity measurements on ceramic materials, *The Old Potter's Almanack* 19 (2014) 18–25.
- [5] C. Di Benedetto, P. Cappelletti, M. Favaro, S.F. Graziano, A. Langella, D. Calcaterra, A. Colella, Porosity as key factor in the durability of two historical building stones: Neapolitan Yellow Tuff and Vicenza Stone, *Eng. Geol.* 193 (2015) 310–319.
- [6] C. Hall, W.D. Hoff, *Water Transport in Brick, Stone and Concrete*, CRC Press: Taylor and Francis Group, 2009.
- [7] K.K. Aligizaki, *Pore Structure in Cement-based Materials. Testing, Interpretation and Requirements*, Taylor and Francis Group, 2006.
- [8] V. Cnudde, M.N. Boone, High-resolution X-ray computed tomography in geosciences: a review of the current technology and applications, *Earth-Sci. Rev.* 123 (2013) 1–17.
- [9] N. Cueto, D. Benavente, J. Martínez-Martínez, M.A. García-del-Cura, Rock fabric, pore geometry and mineralogy effects on water transport in fractured dolostones, *Eng. Geol.* 107 (2009) 1–15.
- [10] S. Siegesmund, H. Dürrast, Physical and mechanical properties of rocks, in: S. Siegesmund, R. Snethlage (Eds.), *Stone in Architecture, Properties, Durability*, Springer, London 2014, pp. 97–225.
- [11] L.M. Anovitz, D.R. Cole, Characterization and analysis of porosity and pore structure, *Rev. Mineral. Geochem.* 80 (2015) 161–164.
- [12] G. Lu, G.Q.M. Lu, Z.M. Xiao, Mechanical properties of porous materials, *J. Porous Mater.* 6 (1999) 359–368.
- [13] R.A. Dorey, J.A. Yeomans, P.A. Smith, Effect of pore clustering on the mechanical properties of ceramics, *J. Eur. Ceram. Soc.* 22 (2002) 403–409.
- [14] J. Seuba, S. Deville, C. Guizard, A.J. Stevenson, Mechanical properties and failure behavior of unidirectional porous ceramics, *Sci. Report.* (2016) 1–11.
- [15] B.D. Zdravkov, J.J. Čermák, M. Šefara, J. Janků, Pore classification in the characterization of porous materials: a perspective, *Cent. Eur. J. Chem.* 5 (2007) 385–395.
- [16] C. Rodríguez-Navarro, Técnicas de análisis del sistema poroso de un material pétreo ornamental, *Cuadernos Técnicos n. 2: "Técnicas de diagnóstico aplicadas a la conservación de los materiales de construcción en los edificios históricos"*, Junta de Andalucía, Consejería de Cultura 1996, pp. 51–65.
- [17] C. Rodríguez-Navarro, E. Sebastián, Técnicas de análisis del sistema poroso de materiales pétreos ornamentales: usos y limitaciones, *Ingeniería Civil* 96 (1994) 130–142.
- [18] S. Galaup, Y. Liu, A. Cerepi, New integrated 2D–3D physical method to evaluate the porosity and microstructure of carbonate and dolomite porous systems, *Microporous Mesoporous Mater.* 154 (2012) 175–186.
- [19] O. Rozenbaum, 3-D characterization of weathered building limestones by high resolution synchrotron X-ray microtomograph, *Sci. Total Environ.* 409 (2011) 1959–1966.
- [20] A.B. Abell, K.L. Willis, D.A. Lange, Mercury intrusion porosimetry and image analysis of cement-based materials, *J. Colloid Interface Sci.* 211 (1999) 39–44.
- [21] G. Barbera, G. Barone, V. Crupi, F. Longo, G. Maisano, D. Majolino, P. Mazzoleni, S. Raneri, J. Teixeira, V. Venuti, A multi-technique approach for the determination of the porous structure of building stone, *Eur. J. Mineral.* 26 (2014) 189–198.
- [22] V. Cnudde, A. Cwirzen, B. Masschaele, P.J.S. Jacobs, Porosity and microstructure characterization of building stones and concretes, *Eng. Geol.* 103 (2009) 76–83.
- [23] Labus M. Rock porosity in the historical monuments preservation. *Civil and Environmental Engineering Reports* 2009; N. 3.
- [24] B. Bai, R. Zhu, S. Wu, W. Yang, J. Gelb, A. Gu, X. Zhang, L. Su, Multi-scale method of Nano(Micro)-CT study on microscopic pore structure of tight sandstone of Yanchang Formation, Ordos Basin, *Pet. Explor. Dev.* 40 (Issue 3) (2013).
- [25] S.P. Rigby, R.S. Fletcher, S.N. Riley, Characterisation of porous solids using integrated nitrogen sorption and mercury porosimetry, *Chem. Eng. Sci.* 59 (2004) 41–51.
- [26] C. Coletti, G. Cultrone, L. Maritan, C. Mazzoli, How to face the new industrial challenge of compatible, sustainable brick production: study of various types of commercially available bricks, *Appl. Clay Sci.* 124–125 (2016) 219–226.
- [27] R. Pirard, C. Alié, J.P. Pirard, Characterization of porous texture of hyperporous materials by mercury porosimetry using densification equation, *Powder Technol.* 128 (2002) 242–247.
- [28] F. Moro, H. Böhni, Ink-bottle effect in mercury intrusion porosimetry of cement-based materials, *J. Colloid Interface Sci.* 246 (2002) 135–149.
- [29] H. Giesche, Mercury porosimetry: a general (practical) overview, *Part. Part. Syst. Charact.* 23 (2006) 9–19.
- [30] S. Diamond, Mercury porosimetry: an inappropriate method for the measurement of pore size distributions in cement-based materials, *Cem. Concr. Res.* 30 (2000) 1517–1525.
- [31] UNI EN 13755, Natural Stone Test Methods - Determination of Water Absorption at Atmospheric Pressure, CNR-ICR, Rome, 2008.
- [32] NORMAL 29/88, Misura dell'indice di asciugamento (drying index), CNR-ICR, Rome, 1988.
- [33] UNI EN 1925, Natural Stone Test Methods - Determination of Water Absorption Coefficient by Capillarity, CNR-ICR, Rome, 2000.
- [34] K.S.W. Sing, D.H. Everett, R.A.W. Haul, L. Moscou, R.A. Pierotti, J. Rouquérol, T. Siemieniowska, Reporting physisorption data for gas/solid systems with special reference to the determination of surface area and porosity, *Pure Appl. Chem.* 57 (1985) 603–619.
- [35] J.C. Groen, L.A.A. Peffer, J. Pérez-Ramírez, Pore size determination in modified micro- and mesoporous materials. Pitfalls and limitations in gas adsorption data analysis, *Microporous Mesoporous Mater.* 60 (2003) 1–17.
- [36] K.S.W. Sing, The use of nitrogen adsorption for the characterisation of porous materials, *Colloids Surf. A Physicochem. Eng. Asp.* 187–188 (2001) 3–9.
- [37] W.S. Rasband, ImageJ, U.S. National Institutes of Health, Bethesda, Maryland, USA. <http://imagej.nih.gov/ij/>, 1997–2015.
- [38] W. Sun, T. Chen, C. Chen, J. Li, A study on membrane morphology by digital image processing, *J. Membr. Sci.* 305 (2007) 93–102.
- [39] E.C. Crawford, J.K. Mortensen, An ImageJ plugin for the rapid morphological characterization of separated particles and an initial application to placer gold analysis, *Comput. Geosci.* 35 (2009) 347–359.
- [40] C. Grove, D.J. Jerram, jPOR: an ImageJ macro to quantify total optical porosity from blue-stained thin sections, *Comput. Geosci.* 37 (2011) 1850–1859.
- [41] C. Noirel, Resolving time-dependent evolution of pore-scale structure, permeability and reactivity using X-ray microtomography, *Rev. Mineral. Geochem.* 80 (2015) 247–285.
- [42] T. Hildebrand, P. Rügsegger, A new method for the model independent assessment of thickness in three dimensional images, *J. Microsc.* 185 (1997) 67–75.
- [43] E. Remy, E. Thiel, Medial axis for chamfer distances: computing look-up tables and neighbourhoods in 2D or 3D, *Pattern Recogn. Lett.* 23 (2002) 649–661.
- [44] S. Storck, H. Bretinger, W.F. Maier, Characterization of micro- and mesoporous solids by physisorption methods and pore-size analysis, *Appl. Catal. A Gen.* 174 (1998) 137–146.
- [45] J. Rouquerol, D. Avnir, C.W. Fairbridge, D.H. Everett, J.H. Haynes, N. Pernicore, J.D.F. Ramsey, K.S.W. Sing, K.K. Unger, Recommendations for the characterization of porous solids, *Pure Appl. Chem.* 66 (1994) 1739–1758.
- [46] F.L.X. Liu, J. Xiong, L. Liang, Investigation of pore structure and fractal characteristics of organic rich Yanchang formation shale in central China by nitrogen adsorption/desorption analysis, *J. Nat. Gas Sci. Eng.* 22 (2015) 62–72.
- [47] W. De Boever, H.D. Derluyn, L. Van Hooerbeke, V. Cnudde, Data-fusion of high resolution X-ray CT, SEM and EDS for 3D and pseudo-3D chemical and structural characterization of sandstone, *Micron* 74 (2015) 15–21.